

Dynamically Reconfigurable Microwave Circuits Leveraging Abrupt Phase-Change Material

David Connelly, *Student Member, IEEE*, Jonathan Chisum, *Senior Member, IEEE*

Abstract—This article proposes a concept for dynamically reconfigurable distributed microwave circuits by leveraging the abrupt conductivity transition in phase-change materials (PCM). Metallic surface-inclusions ($\ll \lambda$) are embedded in the PCM film—vanadium dioxide (VO_2)—to provide low-loss and reconfigurability. To validate this concept, a variety of co-planar waveguide transmission lines are designed and fabricated with metallic surface-inclusions in VO_2 films, and the lines' performance are characterized up to 50 GHz. The measured results are used to develop a transmission-line based model and an equivalent circuit model of the VO_2 with surface-inclusions to aid in the rapid design of new structures. Additionally, an electromagnetic model was developed and indicates that loss can be close to that of conventional metallic distributed circuits with 100 to 200 nm thick VO_2 films. With these thicker films, two practical realizations of this concept were designed and simulated: a tunable dipole from 2.13 to 9.07 GHz and a tunable triple-stub matching network from 5 to 40 GHz with high $|\Gamma|$. Therefore, the proposed method appears viable for the realization of arbitrary programmable distributed circuits and antennas in the microwave and low-millimeter-wave bands.

Index Terms—vanadium dioxide, phase-change material, MIT, IMT, material characterization, millimeter wave, co-planar waveguide, reconfigurable antennas

I. INTRODUCTION

DISTRIBUTED microwave circuits and antennas derive their functionality and performance from their geometry with respect to an electromagnetic wavelength. Such geometries are typically defined through a material contrast in order to efficiently guide, confine, radiate or otherwise manipulate electromagnetic energy. At microwave and millimeter-wave frequencies, the material contrast for passive microwave circuits (e.g., microstrip, co-planar waveguide) and antennas (e.g., dipoles, loops, bow-ties, spirals, patches, etc.) is predominantly realized through geometric patterning of metals on insulating substrates. Because metallic geometry is defined at fabrication time, microwave circuits and antennas are not field-reconfigurable. And yet, nearly every other electrical component from a microprocessor to a Field Programmable Gate Array (FPGA) to a switched analog circuit is field-programmable on some level. It is the fundamental link between functionality and geometry which makes the realization of programmable microwave circuits very challenging. In order to realize fully programmable distributed microwave circuits and antennas, there is a need to locally and dynamically set a circuit's conductivity between that of a metal and that of an insulator.

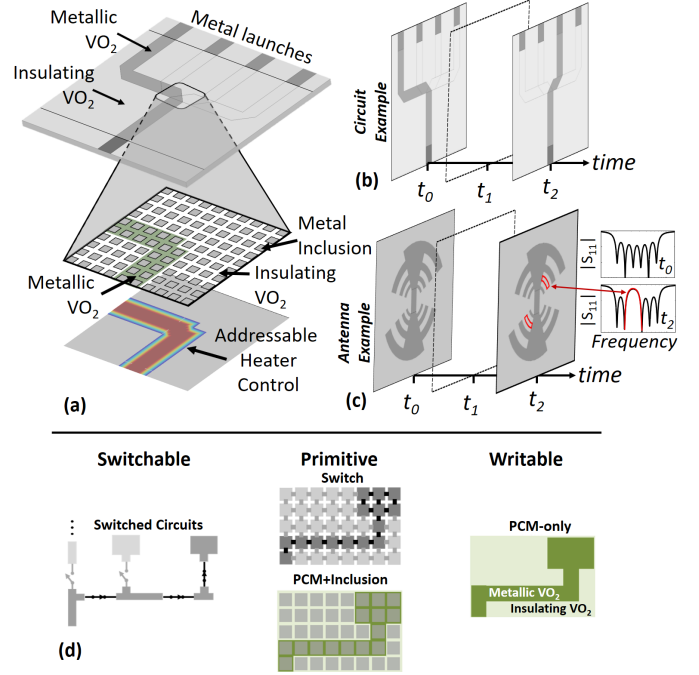


Fig. 1. (a) CONCEPT: VO_2 film on a microwave substrate is patterned with conductive surface-inclusions to reduce loss. Regions of metallic- and insulating- VO_2 are defined (here, by a heater array) to create a distributed circuit or antenna. (b) *Distributed circuit*: event at t_1 triggers reconfiguration of a switch matrix from output one to three. (c) *Antenna scenario*: a log-periodic tooth antenna at t_0 exhibits a wideband input match (inset black $|S_{11}|$ trace). An interference source is detected at time t_1 which triggers reconfiguration and removal of one set of resonant teeth (outlined in red). The input match at t_2 exhibits a notch (red arrow) to reduce interference. (d) Reconfigurable RF circuits can be realized along a continuum from coarsely switched functional circuits (e.g. switch matrix and antenna array) to large arrays of programmable, interconnected conductive surface-inclusions to fully writable PCMs. This article examines the feasibility of metal surface-inclusions in a VO_2 film (“PCM+Inclusion”) to reduce the loss of the “Writable” VO_2 PCM-only approach.

In this article we will present a concept for the dynamic reconfiguration of microwave circuits (including antennas) which leverages the abrupt conductivity transition in phase-change materials (PCM), as depicted in Fig. 1(a).

The family of PCMs, including vanadium dioxide VO_2 [1], [2] and germanium telluride (GeTe) [3], has the ability to change its state from insulating to metallic via several mechanisms, including local heating and even localized illumination with high energy (UV) light. PCMs have been used to realize reconfigurable RF circuits and antennas based upon switches [4], [5], tunable capacitors [6] and with them, tunable filters [6]. However, these approaches only take advantage of the con-

The authors are with the Department of Electrical Engineering, University of Notre Dame, Notre Dame, IN, 46556 USA (e-mail: dconnel7@nd.edu, jchisum@nd.edu).

ductivity transition as a switch mechanism in statically-defined distributed circuits and have stopped short of realizing fully programmable conductor geometry for distributed circuits. The possibility of locally imprinting metallic states across an entire VO₂ film for programmable circuits was first suggested in [7], but neither details nor demonstrations have been offered. One of the challenges of such an approach is that the metallic-state conductivity of VO₂ is two orders of magnitude lower than that of a typical metal ($\sigma_{\text{VO}_2} \approx 10^5 \text{ S/m}$). It is worth noting that NiCr, a material typically used to fabricate microwave resistors [8], has a conductivity on the order of 10^5 S/m , so even in the metallic state, VO₂ behaves more like a thin-film resistor than like a thin metallic conductor.

Past efforts to achieve a programmable conducting surface generally fall into two categories: either patterning a PCM film with a spatially programmable heater array as was simulated in [9], [10], or interconnecting conducting regions with switches. The conducting regions are either traditional microwave structures such as patch antennas [11], [12] or dipole arrays [13], or they are sub-wavelength metallic structures as proposed in [14]. This continuum is depicted in Fig. 1(d) with writable PCM-only films on the right and switch-interconnected traditional microwave structures on the left.

Pure PCM thin films (Fig. 1(d): “Writable”) have insufficient conductivity in the metallic state and thus result in significant loss through microwave structures. For VO₂ film thickness and conductivity of 35 nm and 10^5 S/m , insertion loss is 35–100 dB/mm across 1–50 GHz, rendering this approach infeasible for distributed circuits and antennas. However, if high quality ($> 10^5 \text{ S/m}$) films of significant thicknesses (on the order of a skin-depth) become possible, then a pure VO₂ approach could be considered. The opposite end of the reconfigurable continuum consists of interconnected conductive regions with electrical switches (Fig. 1(d): “Switchable”) and suffers from poor spatial resolution and complex switch routing which interacts electromagnetically with the programmed structure.

In between these two approaches is a third option (Fig. 1(d): “Primitive: PCM+Inclusion”), where metal is deposited discretely as small ($\ll \lambda$), isolated surface-inclusions over a film of PCM material in order to raise the effective conductivity. This concept was proposed in [14] but was not demonstrated or studied in detail. The PCM film can change into a metallic state with either spatially controlled heating (e.g., with a discrete micro-heater array or with a scanned infrared laser) or by raster scanning an ultraviolet laser of sufficient energy level [7]. By such means, the control mechanism is displaced from the electromagnetic structure minimizing electromagnetic interaction between the two.

Figure 1(a) shows the proposed concept in which a phase-change material, here a VO₂ film, containing metallic surface-inclusions is placed in close proximity to a thermal control plane—here a heater array—which is used to thermally bias the VO₂ film in specified regions. The result is a region of metallic VO₂ (indicated as green) where the localized temperature is above the transition temperature ($\sim 68^\circ\text{C}$) within the otherwise insulating VO₂ (clear) regions. Key to the success of such an approach is the abrupt transition of VO₂ conductivity—the insulating to metallic VO₂ conductivity ratio

is 10^4 within approximately 4°C [15], [16]—requiring only a small variation in control temperature profile to switch adjacent cells on an off. Further, this abrupt transition occurs in less than one microsecond [17]. This concept can be used to realize dynamically programmable distributed circuits (Fig. 1(b)) and even programmable and reconfigurable antennas (Fig. 1(c)).

Both Fig. 1(a) and (b) show an example of a programmable distributed circuit: a single-pole, four-throw (SP4T) switch realized by programming a transmission line between the common and the output port of interest. Figure 1(b) shows an hypothetical time-sequence wherein the common port of the distributed SP4T switch is switched from output port 1 at time t_0 to output port 3 at time t_2 due to a reconfiguration event starting at time t_1 . While the benefit of such a realization may not be obvious with an SP4T switch, the benefit becomes clear for a larger number of series switches in each path which results in performance degradation due to reflections and switch loss. In contrast, the programmable switch matrix could have low loss regardless of the switch matrix complexity or function (e.g., blocking and non-blocking).

Figure 1(c) shows that the same concept can be used to realize programmable antennas as well. Here, a toothed log-periodic antenna is reconfigured at time t_1 in response to a detected interference source. A pair of teeth with resonance frequency corresponding to the interference frequency is omitted from the antenna (as in [18]) to produce a rejection band in the antenna’s response. Such a reconfigurable antenna would be useful for cognitive radios in congested environments and for electronic warfare sensors. These two examples illustrate the vast number of possible circuits and antennas one could realize with such a system.

Unfortunately, the necessary integration of PCM and metallic surface-inclusions in order to overcome significant RF loss introduces a trade-off between reducing loss in the metallic state (ON-state) and increasing isolation in the insulating state (OFF-state). Capacitive coupling between metal surface-inclusions in regions of insulating VO₂ results in reduced isolation that degrades with increasing frequency. Effectively, the boundary between conducting and insulating regions of the reconfigurable surface becomes poorly defined. To achieve a low-loss distributed circuit, the percentage of metal must be high and yet, to achieve sufficient reconfigurability, the percentage of metal must be small enough so as to present a well-defined and finely discretized reconfigurable current path.

The purpose of this article is to provide the first demonstration of microwave performance for a VO₂ structure with metallic surface-inclusions here after also referred to as inclusions in order to i) determine the feasibility of such a structure for distributed circuits and antennas, ii) explore the trade-off between loss and isolation versus inclusion geometry, iii) to develop models for design and simulation purposes, and iv) to demonstrate reconfigurable circuits with this concept. To this end, we designed and fabricated unit-cells comprising various percentages of VO₂ film and conductive inclusions, and we performed measurements from 10 MHz to 50 GHz. Based on these measurements, we develop models for circuit, transmission-line, and full-wave electromagnetic simulations.

TABLE I
FABRICATED PARAMETERS FOR EACH STRUCTURE (FIG. 2).

Structure	G (μm)	UC (μm)	W / S (μm)	T_{VO_2} / T_{METAL} (nm)
1	1	10	45 / 106.5	17 / 200
2	2	10	45 / 106.5	17 / 200
3	1	100	45 / 106.5	17 / 200
4	2	100	45 / 106.5	17 / 200

The electromagnetic models are based upon low-frequency material parameter extraction and achieve good agreement with measurement except for minimal tuning of these parameters. Parasitic circuit models are developed which explain the difference between ideal distributed circuit elements (e.g., stubs) and the same structures realized with the proposed VO_2 film with metallic inclusions. In order to simplify the structure for fabrication and measurement, we have reduced the two-dimensional (2D) reconfigurable surface to a one-dimensional (1D) reconfigurable transmission line. We note that the models developed from measured 1D structures are still relevant to 2D structures—specifically, full-wave EM model parameters are identical if the VO_2 film quality is the same.

Section II presents the fabricated test structures and section III presents measurements, calibration, de-embedding, unit-cell model extraction, dispersion analysis, and maximum operating frequency. Section IV extends the present work with a discussion of practical requirements on film and metallization thickness for the realization of high-performance structures, as well as a preliminary yet quantitative thermal control study. Section V presents simulated demonstrations of a tunable dipole and triple-stub matching network, and ends with a discussion of a two-dimensional reconfigurable switch matrix. Final conclusions and future work are presented in section VI.

II. SAMPLE FABRICATION

To investigate the trade-off between ON-state loss and OFF-state isolation as a function of unit-cell parameters (Fig. 2) four co-planar waveguides (CPW) with 8 unit-cells were designed and parameterized by unit-cell length (UC) and unit-cell gap (G) as given in Table I and shown in Fig. 3. Gap sizes of 1 and $2\mu\text{m}$ were chosen to facilitate the fabrication of these structures with photolithography but smaller gaps could be fabricated with more advanced processes (e.g., electron-beam lithography). Unit-cell lengths of $10\mu\text{m}$ and $100\mu\text{m}$ were chosen to vary the ratio of metal to VO_2 in each unit-cell. The $100\mu\text{m}$ unit-cell is expected to exhibit lower on-state insertion loss per unit length at the expense of reduced spatial resolution.

A THRU standard to de-embed the launches was also included. Due to the size of the 50 GHz RF probes used in this work ($150\mu\text{m}$ pitch), a transition from CPW geometry (S, W) = (36, 16) μm to (108, 45) μm was necessary to measure larger unit-cell geometries. Since the CPW probe pads and the larger unit-cell cross-sections have a characteristic impedance of 50Ω , a matching network is not needed; instead, we require a mode transition which maintains a 50Ω environment

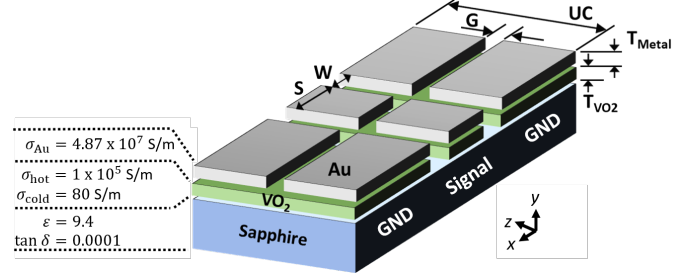


Fig. 2. Unit-cell of a CPW transmission line comprising a VO_2 film (green layer) with gold inclusions (gray layer) on a sapphire substrate (blue layer). The power flow is along the z -axis and the CPW cross-section is in the x - y plane. Fabricated unit-cell parameters (G, UC, S and W) are defined in Table I. The VO_2 conductivities are the final values used to achieve the best fit between electromagnetic models and measurements. Substrate thickness was measured to be $452\mu\text{m}$.

between the mode of the smaller and larger geometries. ADS Momentum was used to confirm that the mode transition maintained $|S_{11}| < -20\text{ dB}$ across the band (0.01–50 GHz).

All experimental work shown here was done using a nominally 20 nm thick VO_2 sample on r -plane sapphire grown using the method of [15] at Pennsylvania State University. Waveguides were patterned on this sample using the University of Notre Dame Nanofabrication Facility. The sample was patterned by photolithography using nLOF 2020 photoresist and the oxide etched in a Reactive Ion Etcher (RIE) using tetrafluoromethane (CF_4) as the etching agent. Lift-off was performed with Remover PG at 80°C after electron-beam evaporating 20 nm of palladium (seed layer) and 180 nm of gold (Au). Palladium was chosen instead of other seed layers, such as titanium, because it does not scavenge the oxygen in the film (which would increase conductivity in the OFF-state). The resulting structures are shown in Fig. 3. The oxide was etched everywhere except underneath and in-between the metal inclusions (Fig. 3a). There is no oxide underneath the launches. The film was etched to eliminate the need to include a micrometer heater array design. This way, the entire sample could be heated or cooled to induce the phase change of VO_2 in the un-etched regions.

Typical cleanroom processes, when performed for extended periods of time, seem to affect the quality (stoichiometry), thickness, and conductivity of VO_2 [19]. The potentially detrimental processes utilized on the sample presented in this paper include cleaning with RF oxygen plasma, rinses with photoresist removal agents and de-ionized water, and heating (max. 110°C). However, the processing time required for this sample was very brief: seconds or minutes instead of the hours taken in the investigation in [19]. Additionally, the film's DC conductivity in the ON and OFF state was measured before and after sample fabrication using a van der Pauw method. The results are $\sigma_{\text{ON}} = 3.61 \times 10^5\text{ S/m}$ and $\sigma_{\text{OFF}} = 95.3\text{ S/m}$ pre-fabrication, which is a $\Delta\sigma = 3.58$ orders of magnitude. Post-fabrication measurements yield $\sigma_{\text{ON}} = 1.65 \times 10^5\text{ S/m}$ and $\sigma_{\text{OFF}} = 188\text{ S/m}$, which is a $\Delta\sigma = 2.94$ orders of magnitude. Thus, there appears to be a slight degradation of the sample's conductivity range. A film-thickness measurement was taken before processing with a 632.8 nm ellipsometer and found to

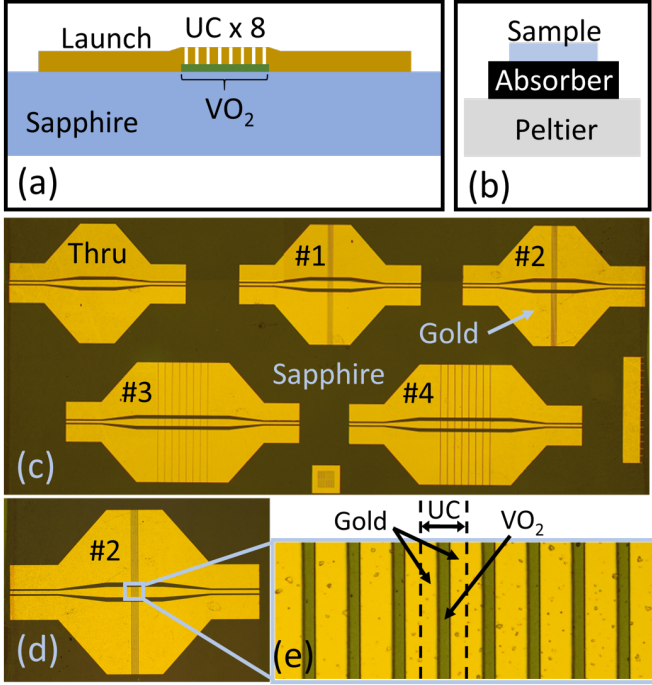


Fig. 3. (a) Side-view of a representative structure that comprises VO₂ underneath all 8 UC but not under the launches. (b) The sample was measured using a carbon-impregnated AlN absorber to remove from the waveguides any possible ground-plane effects, and the sample was heated using a thermoelectric Peltier heater. (c) An overview photograph of the fabricated structures including a THRU standard for de-embedding launches and four structures with varying UC length and gap size. Structures labeled with sample number #1–#4 have dimensions listed in Table I. Close-ups of a structure identifying the unit-cell are provided in (d) and (e).

be $T_{VO_2} = 18.26 \text{ nm}$ using a measured index of refraction published in [7]. A measurement was taken post-processing with an atomic force microscope and found to have an average thickness of 17 nm. The final material values used in the electromagnetic model that best fit the measured s-parameters are $T_{VO_2} = 17 \text{ nm}$, $\sigma_{ON} = 10^5 \text{ S/m}$ and $\sigma_{OFF} = 80 \text{ S/m}$. The conductivity of gold was also measured at $\sim 25^\circ\text{C}$ and found to be $\sigma_{Au} = 4.87 \times 10^7 \text{ S/m}$.

III. MEASUREMENTS AND UNIT-CELL MODELING

A. Calibration and De-embedding

Once the fabrication was complete, s-parameter measurements were taken well above and below the VO₂ transition temperature of $\sim 68^\circ\text{C}$ (hot: $\sim 85^\circ\text{C}$, cold: $\sim 25^\circ\text{C}$) from 10 MHz to 50 GHz with an IF bandwidth of 100 Hz using a Keysight PNA. The sample temperature was measured by a Fluke IR meter and heated well beyond the temperature at which s-parameters stabilized. The sample was placed on a carbon-impregnated AlN absorber (Fig. 3b) to eliminate any possible ground effects due to the metal chuck of the probe station.

While a multi-line calibration kit (e.g., multi-line TRL) would enable s-parameter measurements calibrated to the edge of the 8 unit-cells, limited space on the VO₂ sample chip prevented patterning more than a single THRU standard. Therefore, the measurement setup's systematic errors were

calibrated out up to the probe tips using LRRM standards on an impedance standard substrate (ISS) and launches were de-embedded with an assumption of symmetry. However, the ISS has different pad parasitics than the fabricated sample: the ISS has different fringe (shunt) capacitance due to different dielectric constant and waveguide dimensions, and different series inductance and contact resistance due to thicker metallization and different waveguide dimensions. While it is not straightforward to de-embed all the remaining pad parasitics, de-embedding the contact resistance is simple. At DC, a transmission line is simply a series resistor R , whose ABCD matrix directly gives this resistance and is of the following form:

$$\begin{bmatrix} A & B \\ C & D \end{bmatrix} = \begin{bmatrix} 1 & R \\ 0 & 1 \end{bmatrix} \quad (1)$$

At frequencies slightly higher than DC, the resistance of a short ($\ll \lambda$) transmission line will increase slightly, becoming complex, yet will remain an excellent representation of the line. Therefore, the THRU standard was modeled electromagnetically at 10 MHz, the series R was extracted, and the contact resistance was de-embedded. This contact resistance was assumed to be the same for all structures.

To extract the unit-cell response, the whole structure was treated as a linear system of cascaded individual, symmetric structures represented by transmission parameters. In this paper, T represents ABCD parameters. The unit-cell was then solved for using matrix inversion and matrix square root operations.

After removing contact resistance, the launches and (remaining pad parasitics) were de-embedded using

$$[T_{\text{Launch}}] = [T_{\text{Thru}}]^{1/2} \quad (2)$$

by taking the matrix square root of the entire THRU structure and assigning identical left and right launches to the post-processing of all consequent structures:

$$[T_{\text{UCx8}}] = [T_{\text{Launch}}]^{-1} [T_{\text{struct}}] [T_{\text{Launch}}]^{-1} \quad (3)$$

This assumes that the left and right probe landings were exactly repeatable for all structures. This procedure is summarized in Fig. 4. Repeatability is estimated to be within $\pm 15 \mu\text{m}$, which corresponds to a phase-shift of $\pm 2.1^\circ$ at 50 GHz. Additionally, de-embedding launches with pad parasitics taken from a single THRU measurement produces artifacts in the data, as will be explained in detail in section III-B.

To obtain individual unit-cell parameters, the remaining 8 unit-cell structure was processed using (4). Since taking the matrix square root is equivalent to obtaining the parameters for half the original length, taking the matrix square root 3 times gives parameters for $\frac{1}{2^3} = \frac{1}{8}$ length or one unit-cell; this is the advantage of measuring lengths that are powers of 2.

$$\begin{aligned} [T_{\text{UCx4}}] &= [T_{\text{UCx8}}]^{1/2} \\ [T_{\text{UCx2}}] &= [T_{\text{UCx4}}]^{1/2} \\ [T_{\text{UC}}] &= [T_{\text{UCx2}}]^{1/2} \end{aligned} \quad (4)$$

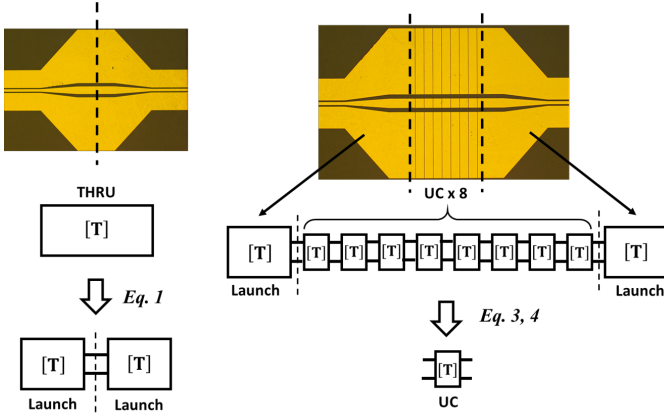


Fig. 4. Diagram illustrating de-embedding and unit-cell extraction from (2), (3), and (4). All blocks are represented by their respective transmission matrix T .

The assumption here is that there are no differences between unit-cells; in reality, any existing differences due to fabrication are averaged across all unit-cells.

B. Results and Modeling

Using the above approach, the unit-cell s -parameters of all structures were de-embedded. In order to understand the unit-cell response in detail, we first focus on a single structure, #2 (Table I) with a $2\text{ }\mu\text{m}$ gap and $10\text{ }\mu\text{m}$ unit-cell length, and then discuss the other structures. Figure 5 shows the measured (solid) and simulated (dotted) s -parameters of the de-embedded unit-cell for structure #2 in metallic and insulating states (labelled as “ON” and “OFF”, respectively). A comparison of all structures may be seen in Fig. 6. Both electromagnetic models (Method of Moments) and circuit models were obtained using industry-standard simulation tools. The electromagnetic model was based on the measured VO_2 thickness and conductivities (section II) and adjusted slightly to obtain good fits of the measured s -parameters as specified in Sec. II above and repeated here for convenience. The final material values used in the electromagnetic model that best fit the measured s -parameters are $T_{\text{VO}_2} = 17\text{ nm}$, $\sigma_{\text{ON}} = 10^5\text{ S/m}$ and $\sigma_{\text{OFF}} = 80\text{ S/m}$. The conductivity of gold was also measured at $\sim 25^\circ\text{C}$ and found to be $\sigma_{\text{Au}} = 4.87 \times 10^7\text{ S/m}$. These are all included in the EM model in Fig. 2. The actual fabricated dimensions of the waveguide were also accounted for: $S = 106.5\text{ }\mu\text{m}$ and $W = 45\text{ }\mu\text{m}$. The circuit model of Table II was fit to the measured s -parameters across the entire band, and the resulting values are summarized in Table II. The ON and OFF-state resistance of the VO_2 is modeled as a series resistance R_{VO_2} , and the gap capacitance is modeled by a series capacitance C_{GAP} and shunt capacitances C_{sh} representing fringing fields from the CPW signal line to ground planes [20], [21]. In addition to the VO_2 unit-cell, Fig. 5 shows the s -parameters of a simulated, realistic $10\text{ }\mu\text{m}$ pure metal line (black solid, circle marker)—the ideal response to which the ON-state VO_2 with inclusions should be compared—and a simulated, realistic $4\text{ }\mu\text{m}$ metal open stub with fringe capacitance (black solid, diamond marker)—the ideal response to which the OFF-state

VO_2 with inclusions should be compared. This comparison indicates how well this reconfigurable concept compares to a traditional, non-reconfigurable circuit.

In general, the measured and simulated values are in good agreement, indicating that the VO_2 film parameters used in the EM models as summarized in Fig. 2 are valid and useful for new designs. The measured transmission, S_{21} , undergoes a change of approximately four orders of magnitude between the ON and OFF states; however, the ON-state insertion loss is as much as 0.87 dB/UC up to 50 GHz . As will be discussed below, this loss is dominated by the resistance of the VO_2 film due to the limited film thickness, 17 nm , used in these proof-of-concept structures. The OFF-state isolation is better than 40 dB at low frequencies, but as frequency increases, the isolation follows a nearly perfect series $R \parallel C$ response (i.e., the isolation matches that of a parallel $R \parallel C$ network in series with the two ports of the VNA). These observations indicate that there is a fundamental trade-off between loss and isolation across the unit-cell gap but that increased film thickness can mitigate the loss, as will be discussed in section IV. However, before further discussion of the measurements, we address the presence of three artifacts in the measurement.

There are three observable resonances (1.5 , 15.35 , and 26.4 GHz) in the measured results, and each of these correspond to calibration and de-embedding limitations, not to the unit-cell structures. The resonance seen near 26.4 GHz is due to differences in pad parasitics between the ISS structures and the test structures on sapphire which manifest when computing (2). Due to limited space on the VO_2 sample, the THRU standard was limited to 2.5 mm long, where it is $\frac{\lambda}{2}$ at 26.4 GHz ($\epsilon_{\text{eff}} = 5.15$). A transmission line, at multiples of $\frac{\lambda}{2}$, does not transform the load impedance. Instead, the line will appear transparent, with exception of accumulated phase and loss. Since the THRU standard is terminated with pad parasitics and $50\text{ }\Omega$ (calibrated system) load, the input impedance at 26.4 GHz will be simply the parasitics and calibrated system. Therefore, any method of de-embedding launches from a THRU that still has parasitics will cause a resonance to appear [22]–[24]. When modeling this entire structure and de-embedding using the same procedure as in Fig. 4, the same resonance appears at 26.4 GHz . Adjusting the launch length of the simulated THRU standard to 0.25 mm causes the resonance to be pushed to a much higher frequency outside the measurement range. Therefore, no resonance appears in the simulated curves in Fig. 5.

The S_{21} of the VO_2 unit-cell of structure 2 (Fig. 5(a)) in the ON state is at most -0.867 dB per unit-cell across the entire measured band, while the pure metal unit-cell is at most -0.0022 dB per unit-cell. Obviously, this is impractical; this is the result of very thin VO_2 films (17 nm) and a large unit-cell gap ($2\text{ }\mu\text{m}$). As will be shown later, smaller gaps and thicker films exhibit losses closer to that of a pure metal line, thereby demonstrating potential for this reconfigurable concept to work.

The lines’ phase progressions (Fig. 5(b)) are more similar with $\beta l = 1.03^\circ$ and 1.371° at 50 GHz for a VO_2 and metal unit-cell, respectively. This deviation of the measured VO_2 unit-cell from the pure metallic unit-cell at 50 GHz (and other

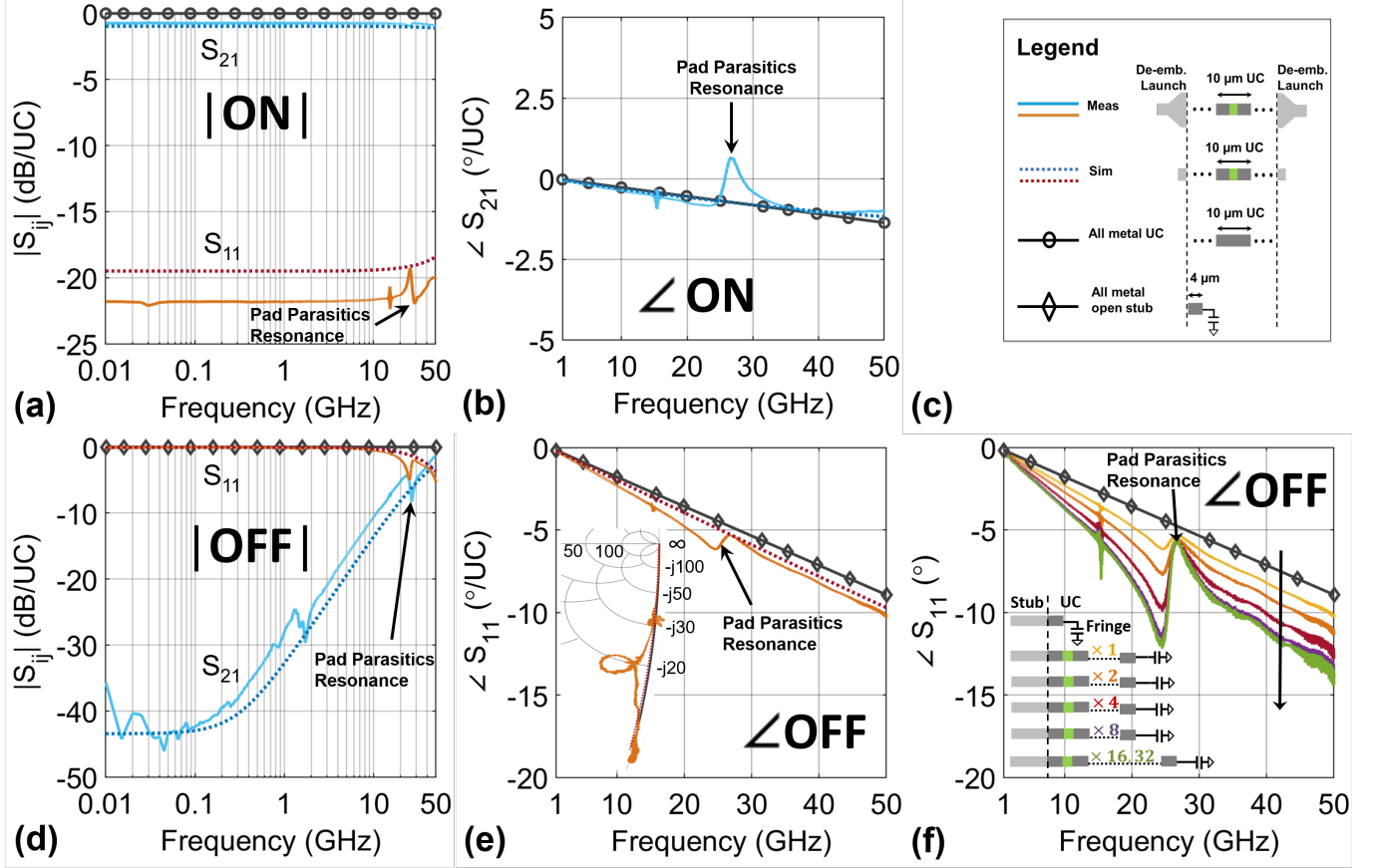


Fig. 5. S-parameters for structure 2 (Table I): solid is measured, dotted is simulated using MoM. Top row (a, b, c) and bottom row (d, e, f) show ON-state and OFF-state results, respectively. Black curves with circular markers for (a) and (b) correspond to S_{21} of a $10\ \mu\text{m}$ pure metallic line. Black curves with diamond markers for (d) and (e) correspond to S_{11} of a $4\ \mu\text{m}$ metallic open stub with fringe capacitance. (c) serves as the legend for the entire figure. (f) shows the phase of the reflection coefficient converging after 16x OFF-state UCs + simulated fringe capacitance are cascaded at the end of a $4\ \mu\text{m}$ stub. Plots (e) and (f) show the 2-port measured OFF-state UCs converted to 1-port measurements, with the second port terminated in simulated fringe capacitance.

frequencies) is partially due to distortion by the pad parasitics nearing the frequency ($52.8\ \text{GHz}$) at which the line is λ . The electromagnetic simulation shows a slight dispersion of the phase for a VO_2 UC, which makes more sense given the significant loss of the oxide.

Nonetheless, low ON-state insertion loss is not the only criterion necessary to render this concept practical: high OFF-state isolation is also essential to create well-defined current paths. The isolation of a VO_2 unit-cell (Fig. 5(d)) in the OFF state is greater than $40\ \text{dB}$ below $200\ \text{MHz}$ and degrades with a slope of $\sim 20\ \text{dB/dec}$ as frequency increases, the same slope as a series capacitor. The high S_{11} indicates the power is primarily reflected, not absorbed, across the entire band. Below $200\ \text{MHz}$, the VO_2 film dominates the insertion loss due to its low conductivity, and above $200\ \text{MHz}$, the unit-cell gap capacitance dominates. In fact, the OFF-state unit-cell is modeled extremely well by a series resistor R_{VO_2} in parallel with a capacitor C_{GAP} , and the values are found in Table II. This means that higher frequencies are worse at confining current to a designed path and allow current to leak into nearby unit-cells. This is extremely relevant to designing antennas, where the current distribution dictates the far field radiation pattern. This is also pertinent to designing the characteristic impedance

of distributed circuits, which is inherently dependent on widths of and gaps between conductors. The characteristic impedance will exhibit an increased frequency dependence, and this must be accounted in the design of these circuits.

Because a VO_2 unit-cell in the OFF-state is supposed to approximate a metallic open stub with fringe capacitance, a comparison of the phase of the reflection coefficient is also very indicative of the OFF-state behavior. In order to compare with a 1-port metallic open stub, the 2-port OFF-state unit-cell was converted to a 1-port measurement. However, the original 2-port OFF-state unit-cell measurement did not include fringe capacitance, so the second port was terminated in a simulated fringe capacitance. In the case of an entire chip of embedded metallic inclusions in a PCM film, the OFF-state phase of the unit-cell is not only determined by the first OFF-state gap but also by all the consecutive unit-cells which will couple through fringing fields. Each unit-cell will provide isolation but also add slightly to the phase of S_{11} because field lines will also terminate on conductors in distant unit-cells (albeit with diminishing proportion). Fig. 5(f) illustrates this by plotting the reflection coefficient phase for 1 through 32 cascaded UCs in the OFF-state. The phase converges at 16 UCs; it is hidden beneath the 32 unit-cell curve. Therefore,

TABLE II
UNIT-CELL TRANSMISSION LINE AND CIRCUIT PARAMETERS.

Structure (UC / G μm)	Z_o (Ω) ON	α (dB/mm) ON	β (rad/mm) ON	R_{VO2} (Ω) ON / OFF	C_{GAP} (fF) ON&OFF	C_{sh} (fF) ON&OFF
Metal (10/0)	50.6 - j0.520	0.217	2.39	0.0252		
1 (10/1)	101 - j80.5	31.3	4.47	5.92 / 7,288	35.6	0.868
2 (10/2)	128 - j119	46.4	5.69	11.8 / 14,566	34.2	1.56
3 (100/1)	60.4 - j16.9	5.98	2.57	5.91 / 7,465	17.9	0.220
4 (100/2)	64.4 - j28.8	10.3	2.75	11.8 / 15,035	17.3	0.450
Structure (T_{VO2} / G nm): UC = 10 μm						
100/100	56.2 - j6.26	2.52	2.51	0.103 / 2,003	42.1	0.200
100/500	59.9 - j15.6	6.15	2.67	0.506 / 10,000	37.8	0.402
200/100	55.5 - j4.71	1.91	2.47	0.0522 / 1,003	43.3	0.157
200/500	57.9 - j9.99	3.96	2.58	0.254 / 5,010	38.2	0.256

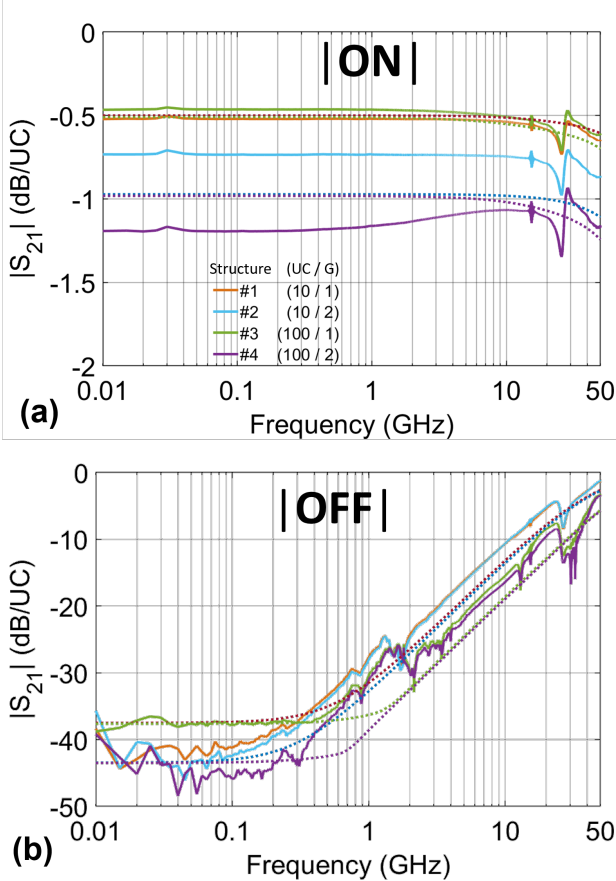
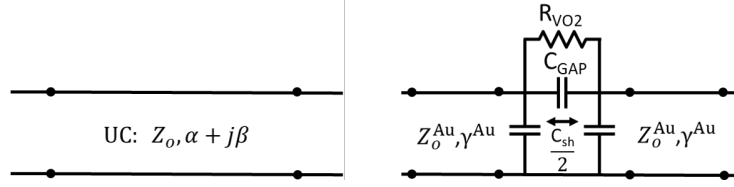


Fig. 6. S-parameters for all fabricated structures (Table I): solid is measured, dotted is simulated using MoM. (a) shows the ON-state results, and (b) shows the OFF-state results.

the total additional phase accumulated by a stub terminated in these OFF-state UCs is dominated by the first 16 UCs and is $\Delta\phi = 5.06^\circ$ at 50 GHz for this structure. If this extra phase were represented by an increase in fringe capacitance, then $\Delta C = 7.6 - 4.97 = 2.63$ fF. This additional capacitance must be considered when designing metallic/PCM-based stubs, such as in matching networks, where the required stub length should be reduced slightly to account for the added capacitance.

All the measured structures are compared together in Fig. 6. Figure 6(a) shows two trends in the ON-state. First, measured (solid curves) structures 1 and 3 have very similar loss even though they are 10 μm and 100 μm long, respectively, because s-parameters are plotted in dB/UC and the gaps are identical. Second, measured structures 2 and 4 show more loss than 1 and 3 due to a larger gap (2 vs 1 μm), but their loss does not double like intuition and simulation (dotted) would predict. This is attributed to non-uniformity in film thickness and/or quality across the sample. Figure 6(b) also shows two trends in the OFF-state. At low frequencies, structures 1 and 3 have less isolation than 2 and 4, although 1 and 3 should be nearly identical as indicated by the simulated curves. Again, this discrepancy is attributed to non-uniformity in the film. At high frequencies, structures 1 and 2 have similar (although not identical) capacitance, whereas structures 3 and 4 have similar capacitance. A change in gap G does not affect the capacitance much because, for this metal thickness and geometry, the capacitance is due mostly to fringing fields: fields not directly in the gap cross-section but beginning and terminating on the metallic inclusions. Structures with the same gap (1 and 3) differ significantly in capacitance C_{GAP} confirming that metal in close proximity to the gap dominates the capacitance instead of the gap (for these gap and line geometries).

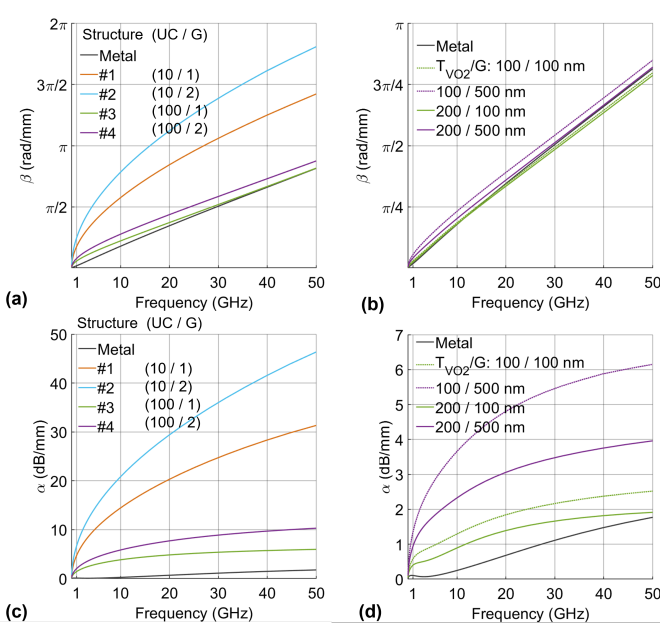


Fig. 7. (a) and (c) Phase and attenuation constant per millimeter as a function of frequency for each of the fabricated 17 nm VO₂ structures. (b) and (d) Phase and attenuation constant per millimeter as a function of frequency for a simulated unit-cell of thicker VO₂ films and smaller gaps.

A transmission line model (bottom left figure in Table II) is extracted from the EM simulation of all fabricated and measured ON-state unit-cells. The attenuation constant, α , and propagation constant, β , are plotted versus frequency in Fig. 7(a) and (c). In general, the very thin VO₂ causes the attenuation constant, α , to be very high compared to a metal-only unit-cell and to increase as the VO₂ percentage increases. There is significant dispersion evident in Fig. 7(a) for structures 1 and 2 (UC = 10 μ m), suggesting that the propagation mode is very different from a quasi-TEM mode; some dispersion is evident for structures 3 and 4 (UC = 100 μ m) but is less than for structures 1 and 2 because of a lower percentage of VO₂ per millimeter. A transmission line model is given at 50 GHz in the top left half of Table II which is useful for design from low-bands to 50 GHz for the 100 μ m unit-cell but it cannot be extrapolated to all lower frequencies for the 10 μ m unit-cell because of the dispersion. In general Fig. 7 should be consulted for accurate modeling of transmission line propagation coefficients.

Thicker films and smaller gaps (bottom left half of Table II), which are discussed more in section IV, bring the attenuation constant to within three times that of metal (Fig. 7(d)), and therefore exhibit minimal dispersion in the phase constant, β (Fig. 7(b)). The attenuation constant follows a square root dependency on frequency. Likewise, under the same conditions that bring α and β closer to ideal, the characteristic impedance, Z_o , will remain similar to a metal unit-cell.

A circuit model (bottom right figure in Table II) is fit to the EM simulation of all ON- and OFF-state unit-cells across the entire band. The metallic portion of each structure is modeled as a traditional transmission line ($Z_o^{\text{Au}}, \gamma^{\text{Au}}$) at each frequency

point, while the VO₂ portion is modeled with a lumped resistor R_{VO_2} and a lumped gap capacitor model for the entire band. The gap capacitor model is assumed to be identical in both ON/OFF states; the C_{sh} was fit in the ON-state and C_{GAP} was fit in the OFF-state. For thick films, the circuit model is a very good fit, particularly the phase of S_{21} for ON-state unit-cells, indicating that any parasitics present due to evanescent modes as a result of the discontinuities are either well represented or negligible. The VO₂ resistance scales linearly with gap, but the capacitance does not. Because the metal is so thin and the gap is so small, fringing fields dominate the capacitance and thus do not scale linearly with gap size. This is discussed more in section IV. The C_{sh} is much smaller than C_{GAP} because the CPW gap W is much larger than the unit-cell gap G . Both these trends are predicted by a FEM model of a single unit-cell.

C. Maximum Operating Frequency

While ON-state insertion loss is relatively low and constant versus frequency up to 50 GHz (see Fig. 6), this does not necessarily indicate these structures are useful up to 50 GHz because OFF-state isolation, which is dominated by capacitance, reduces significantly as frequency increases. In this section we are interested in a rule for maximum operating frequency of the proposed structures. In general, a single OFF-state unit-cell does not need to provide the total desired isolation in order to realize a particular circuit geometry. Rather, unit-cells may be cascaded together to achieve a high degree of total isolation if the unit-cells are small compared to a wavelength. For example, consider that a 10 μ m (100 μ m) unit-cell is $\lambda/20$ at 660 GHz (66 GHz); therefore, many cells can participate in accomplishing the required isolation for frequencies below these values. Consequently, we propose a criterion to determine the maximum operating frequency of the proposed structures based upon the length required to achieve

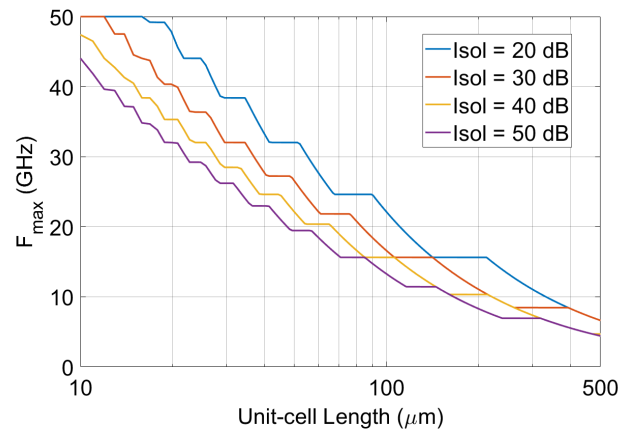


Fig. 8. Maximum operating frequency versus unit-cell length based upon a requirement to achieve 20, 30, 40, and 50 dB of isolation within an electrical length of $\lambda/20$. For the 10 μ m (100 μ m) cells used in this work, $f_{\text{max}} = 45$ GHz (15 GHz) for a 40 dB isolation requirement. R_{ON} and C_{OFF} from the measured 17-nm-thick VO₂ films were used in this calculation but the results are almost the same for thicker films since C_{OFF} ends up dominating the high-frequency response.

a desired isolation in the OFF-state. Specifically, we define the maximum frequency of operation to be that frequency at which the desired isolation is achieved within $\lambda/20$. This means that the correct number of unit-cells and the correct unit-cell length must be selected to achieve the required isolation within $\lambda/20$.

In order to determine the maximum operating frequency f_{max} versus unit-cell length, we first compute the number of unit-cells required to achieve a particular isolation specification (here 20, 30, 40, 50 dB) at a given frequency and then compute the required unit-cell length so that the overall length is less than $\lambda/20$ at the chosen frequency. Figure 8 shows the resulting f_{max} versus unit-cell length using the R_{ON} and C_{OFF} values extracted from measurements of the 17 nm-thick VO_2 films in this work. However, we point out that these curves are very similar for thicker (e.g., 200 nm) films because the high-frequency limit is determined by C_{OFF} . To satisfy a 40 dB isolation requirement, a $10\mu\text{m}$ unit-cell length can operate up to 45 GHz and a $100\mu\text{m}$ unit-cell length can operate up to 14 GHz. Note that the curves are discontinuous at some frequencies because $\lambda/20$ has to be an integer multiple of a unit-cell length in order to meet (or exceed) the isolation requirement. It is worth pointing out that some applications may not require such a stringent isolation spec or they may be robust to vestigial lines longer than $\lambda/20$, in which case the maximum frequency would increase.

IV. PRACTICAL IMPLEMENTATION

A. Improved Electrical Performance

The previous results highlight the need for thicker films and smaller gaps to make this concept feasible. Consequently, two additional $10\mu\text{m}$ unit-cell structures with realizable gap sizes and reasonable film thicknesses are simulated and presented in Fig. 9(a) and (b): $G = 100$ and 500 nm , and $T_{VO_2} = 100$ and 200 nm . Moreover, in these simulations the OFF-state conductivity of VO_2 has been lowered to 5 S/m , which has been the measured conductivity for films above the critical thickness ($\sim 20\text{ nm}$) [15].

As expected, thicker films and smaller gaps dramatically reduce the loss. A film thickness of 200 nm and gap of 100 nm yield at most 0.012 dB/UC insertion loss from 0.01 – 5 GHz and a maximum loss of 0.028 dB/UC at 50 GHz , much closer to the metal's 0.0022 dB/UC , in contrast to 0.867 dB for structure 2. The price paid for this in the OFF-state is reduced isolation: 20 dB/UC from 0.01 – 1 GHz , 11.8 dB/UC at 10 GHz , and 2.3 dB/UC at 50 GHz . The metal thickness for all structures plotted in Fig. 9(a) and (b) was maintained at 200 nm , but the metal thickness can be increased up to $2\mu\text{m}$ without significantly increasing the capacitive coupling between unit-cells. Additional FEM simulations show that, for gap sizes of 0.5 and $1\mu\text{m}$, capacitance is nearly unchanging for a metal thickness up to $2\mu\text{m}$ and increases by 10% for a metal thickness of $5\mu\text{m}$. For a gap size of $0.1\mu\text{m}$, the capacitance increases by 23% for a metal thickness of $2\mu\text{m}$ and by 48% for a metal thickness of $5\mu\text{m}$. The parallel-plate capacitance in the gap is quite small compared to the overall gap capacitance because the fringing fields, not the parallel-plate fields, dominate. When the metal thickness becomes

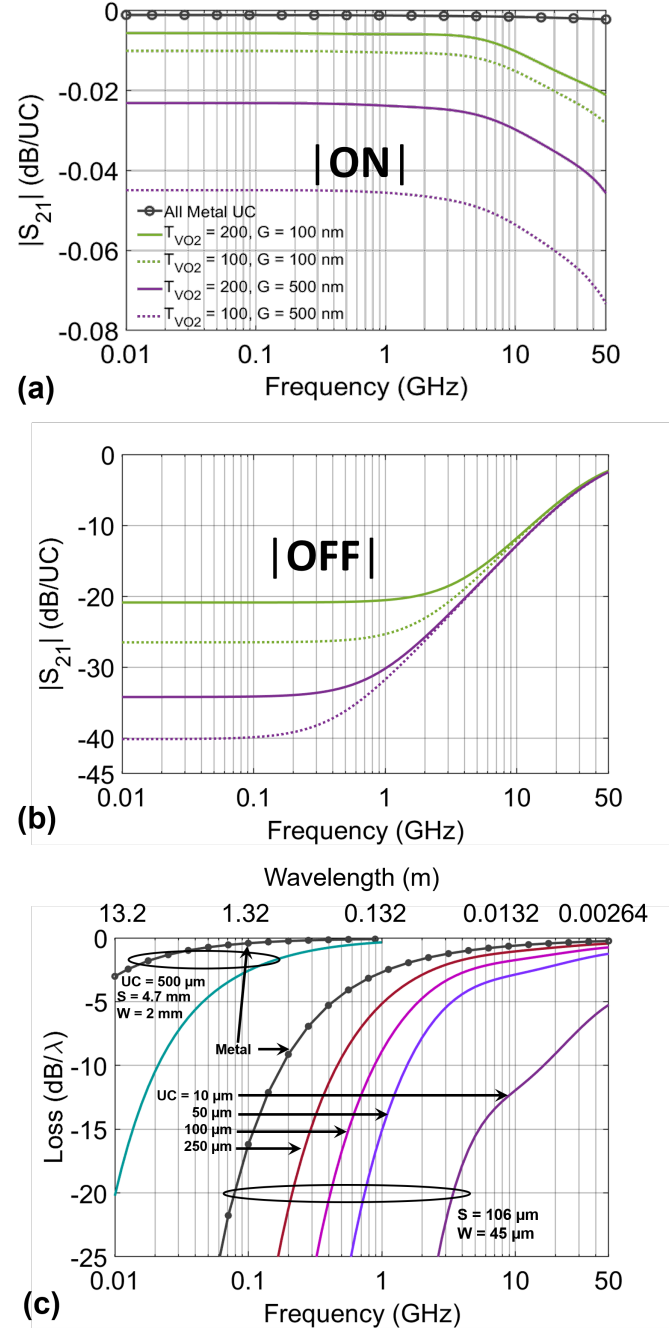


Fig. 9. In order to feasibly design practical low-loss circuits, parametric studies were conducted of T_{VO_2} and G for ON state (a) and OFF state (b). In (c), curves show the $|S_{21}|$ loss for CPW lines of length equal to the corresponding wavelength at each frequency, where the lines comprise unit-cell sizes of 10, 50, 100, or $250\mu\text{m}$. Curves shown are for $T_{VO_2} = 200\text{ nm}$ and $G = 100\text{ nm}$. Metal lines (black, circle marker) are shown for reference. Structures with signal width $S = 106.5\mu\text{m}$ and gap $G = 45\mu\text{m}$ are inherently suited for microwave and millimeter-wave lengths, whereas larger CPW dimensions of $S = 4.7\text{ mm}$ and $G = 2\text{ mm}$ are suited for longer wavelengths. All curves are with $T_{Au} = 2\mu\text{m}$.

large relative to the gap size ($5\mu\text{m}$ metal thickness and $0.1\mu\text{m}$ gap), then the parallel-plate fields begin dominating.

Because distributed circuits are functional at lengths comparable to a wavelength, it is most useful to see the loss incurred per the guided wavelength at each frequency. This is plotted

in Fig. 9(c) for a film thickness of 200 nm and a gap G of 100 nm for several unit-cell sizes (10-purple, 50-violet, 100-magenta, 250-dark-red, and 500-cyan μm). A pure metallic line is shown (black, circle marker) as a reference. Metal thickness for all structures plotted in Fig. 9(c) were increased to $2\text{ }\mu\text{m}$, which is typical for mmICs, to show more realistic losses. In general, the loss per wavelength decreases with increasing frequency because wavelength decreases inversely with frequency, whereas conductor loss increases by the square root of frequency. At 10 GHz, a $10\text{ }\mu\text{m}$ unit-cell has $12\text{ dB}/\lambda$ loss, whereas the 50, 100, and 250 μm UCs have 2.9, 1.74, and $1.06\text{ dB}/\lambda$ loss, much closer to the metal's $0.6\text{ dB}/\lambda$. Thus, the unit-cell length is a very useful degree of freedom so long as the overall isolation specification is met and the application allows for reduced spatial resolution.

Up to now, the CPW geometry used in the measurements and simulations has been quite small in order to maintain a quasi-TEM mode at 50 GHz, but such a small size has prohibitive insertion loss at low frequencies. Thus, a much larger geometry ($S = 4.7\text{ mm}$, $W = 2\text{ mm}$) was simulated to target the band below 1 GHz with a $500\text{ }\mu\text{m}$ unit-cell and plotted (aqua) alongside its metallic reference (black, circular marker). This geometry maintains losses less than $5\text{ dB}/\lambda$ even down to 44 MHz.

B. Thermal Control Considerations

While the primary purpose of this work is to explore the electrical performance of the PCM-metal surface-inclusion concept across the microwave and low-millimeter-wave band, we also provide a preliminary, quantitative study of a thermal control system similar to the heater array depicted in Fig. 1(a), in order to demonstrate the feasibility of such a system. Thermal control by spatial confinement of heat is challenging in thermally conductive substrates such as sapphire, but the use of a highly abrupt insulator-metal phase transition renders this approach feasible. Single crystal VO_2 films, such as the sample utilized in this paper, have a thermal transition width of 4-6 $^\circ\text{C}$ per about 4 decades of conductivity [15], [16]. Beyond the 4 decades of nearly abrupt change the conductivity saturates quickly in the ON state, and in the OFF state the conductivity continues to lower very gradually with decreasing temperature (drops from 16 S/m at $65\text{ }^\circ\text{C}$ to 5 S/m at $25\text{ }^\circ\text{C}$). Thus, we do not expect fluctuations in substrate temperature $\geq 70\text{ }^\circ\text{C}$ or $\leq 66\text{ }^\circ\text{C}$ to significantly affect the reconfigurable circuit parameters.

Nonetheless, because the transition is not instantaneous versus temperature, we have thermally simulated a 1D array of heat sources using an FEM heat-flow simulator (Ansys IcePak) to determine the heat profile in the substrate and the number of unit-cells needed to span the VO_2 transition region. Figure 10 shows the simulation setup and results. Figure 10(a) shows the simulated geometry where control heaters are patterned on the back-side of a sapphire substrate (thickness H : 50, 100, 500 μm) and spaced $100\text{ }\mu\text{m}$ apart. Temperature was monitored along a line at the top of the substrate, where the unit-cell VO_2 would be present. Because VO_2 is nearly fully on above $70\text{ }^\circ\text{C}$, the heaters were specified as constant

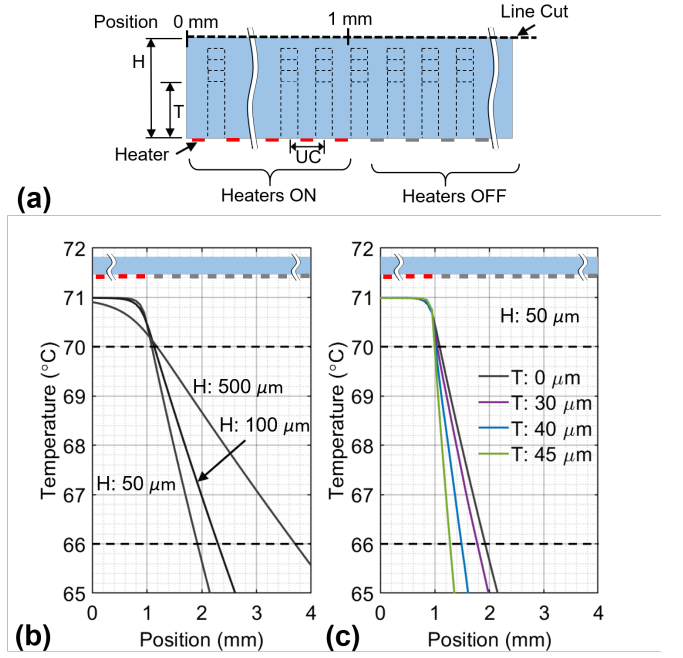


Fig. 10. a) Thermal simulation setup with various sapphire substrate thicknesses (H), and various trench depths (T). Heaters at $71\text{ }^\circ\text{C}$ are placed along the bottom of the substrate up to the 1 mm mark. b) and c) plot thermal profiles vs. distance along top of substrate for various substrate thicknesses and trench depths.

temperature regions at $71\text{ }^\circ\text{C}$. The heaters in Fig. 10(a), (b), and (c) are colored red up to 1 mm to indicate a temperature of $71\text{ }^\circ\text{C}$ and are grayed out after 1 mm because they do not have a temperature condition specified. Horizontal black dashed lines indicate the transition region ($66\text{--}70\text{ }^\circ\text{C}$) of VO_2 to go from ON to OFF.

In order to improve confinement of heat within a unit-cell trenches of various depths were also modeled in the substrate (steep, straight sidewalls are easily realizable with DRIE as in our prior work [25]). In Fig. 10(c), these trench depths are denoted as T in the legend. When $T = 0$ (black curves), no trench was etched. In general, as the substrate is thicker, more distance is required within the transition temperature region. By adding trenches, this adds isolation between each heater and reduces further the required distance to achieve a temperature transition. A trench distance of 90% of H (here, $45\text{ }\mu\text{m}$ for $H = 50\text{ }\mu\text{m}$) is plotted as the best one could achieve, even though this is an impractical percentage to fabricate without compromising the substrate's mechanical integrity. A variety of more reasonable percentages are also shown ranging from 60% to 90% and the distances summarized in Table III.

The transition distance between fully ON and OFF unit-cells adds an effective length and resistance to the line. As a worst case, if we consider these unit-cells in the transition region to be fully on (maximum conductivity), this added length will only begin to matter at the frequency at which the length is $\lambda/20$ (according to the f_{max} criterion we defined above). These frequencies are calculated and given in Table III for each variation in substrate size and trench depth. Specifically, for a $50\text{ }\mu\text{m}$ substrate thickness, the distance required to

TABLE III
THERMAL SIMULATIONS OF HEATER ARRAYS

Substrate (μm)	50	100	500	
Distance for T: $0\mu\text{m}$	0.83 mm	1.16 mm	2.53 mm	
Frequency ($\lambda/20$)	8.00 GHz	5.73 GHz	2.63 GHz	
Substrate $50\mu\text{m}$, T (μm)	0	30	40	45
Distance	0.83 mm	0.73 mm	0.48 mm	0.28 mm
Frequency ($\lambda/20$)	8.00 GHz	9.1 GHz	13.84 GHz	23.72 GHz

transition to fully OFF (low conductivity) is 0.83, 0.73, 0.48, and 0.28 mm, respectively. The corresponding frequency at which these lengths correspond to $\lambda/20$ are 8, 9.1, 13.8, and 23.7 GHz, respectively. In reality, not all these unit-cells are on, but their resistance grows increasingly higher. This adds an additional isolation along the line so that the maximum operating frequency would be higher than that quoted in Tab. III but, in the case of a stub, this additional series resistance would result in a reduction of realizable $|\Gamma|$.

Another consideration for a thermal control system is the significant temperature variation across a substrate due to, for example, hot-spots caused by power dissipation in active components. If such a hot-spot temperature is greater than the critical temperature of 68°C and very close to a VO_2 unit-cell, then the cell may be unintentionally activated. Based on the same thermal simulations on sapphire discussed above, a heat source at 71°C , which is $\Delta T = 46^\circ\text{C}$ above ambient, required 100 mm of distance for the substrate to reach ambient temperature (25°C). This result can be used to estimate that 100 mm is also required between an active component with a junction temperature of 117°C (which is $\Delta T = 46^\circ\text{C}$ above 71°C), and the first OFF-state unit-cell after a heater. In reality, the distance required will be less than this, because the active component's ΔT from ambient (92°C) will increase its heat dissipation rate and cause the temperature to decay faster. Furthermore, in typical scenarios for the proposed VO_2 circuits, the VO_2 would be on a separate passive-only substrate from active devices (e.g., an impedance tuner wire-bonded to a PA). Therefore the sapphire-to-PCB transition would present a thermal discontinuity which would provide significant insulation, further mitigating this issue. Therefore, so long as VO_2 unit-cells are not placed in close proximity to heat sources, this problem can be mitigated.

Fabrication of a heater array should not require expensive or novel clean-room processes since it can be realized with standard lithographic processes and metal depositions (electron-beam evaporation or sputtering). A low-cost solution would be to fabricate the heater array on a separate, thin wafer, since this will eliminate the need for back-side wafer processing of the sample with the VO_2 film. An estimated power consumption from a thermal simulation of heaters on a $50\mu\text{m}$ sapphire reveals that $1.6\mu\text{W}$ was required to heat an area of 0.4mm^2 to 71° . This is similar to thermal simulations in [9] where $1.5\mu\text{W}$ was sufficient to heat 4mm^2 to 87° . Therefore, an estimated $30\mu\text{W}$ would be necessary to heat the reconfigurable dipole and $36\mu\text{W}$ would be necessary for the tunable triple-

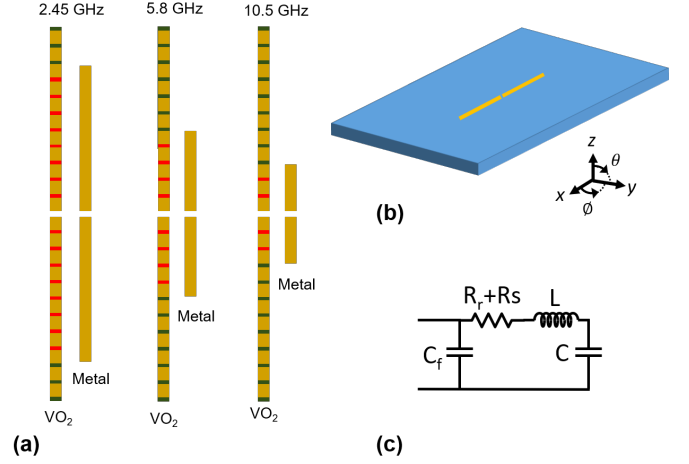


Fig. 11. (a) Simulation setup of three all-metal metal dipoles and three dipoles with VO_2 -metal surface-inclusions at 2.45, 5.8, and 10.5 GHz. Unit cell length is $100\mu\text{m}$, feed gap is $100\mu\text{m}$, and dipole width is $200\mu\text{m}$. VO_2 film thickness is 100nm and gap is 100nm . Neither the dipole dimensions nor the number of unit-cells are to scale. The VO_2 dipoles are loaded with OFF-state unit-cells (dark green). (b) The dipoles were modeled on a sapphire substrate. (c) The circuit model for each dipole consists of a feed capacitance in parallel with a series RLC circuit with values defined in Table IV.

stub matching network presented in section V.

V. APPLICATIONS

As seen in Fig. 8, depending on the unit-cell size the proposed structures could perform well in the 10's of GHz and even up to 45 GHz which opens up a broad range of applications. These include both antenna applications and guided-wave circuits. Just to list a few examples: reflectarrays [26] are often deployed on small satellites because of their compact size and high aperture efficiency. The proposed structures could be used to realize a dynamically reconfigurable version of these surfaces. Similarly, lens antennas are often used for satellite communications [27] due to their high gain and wideband operation. The proposed structures could be used in these switch-beam lens antenna systems to greatly simplify the switch matrix used as a feed network. And of course dynamic matching networks such as stub-tuners [28] could provide for high efficiency operation of power amplifiers under varying load impedance conditions.

As observed in Fig. 8 and 9, the suitable frequency range for a $100\mu\text{m}$ unit-cell is 2 to 14 GHz (40 dB isolation), and for a $250\mu\text{m}$ unit-cell the range is 1 to 12 GHz (20 dB isolation). Thus, two practical reconfigurable circuit realizations in these bands are demonstrated in simulation and presented below: a reconfigurable dipole with $100\mu\text{m}$ unit-cells, and a reconfigurable triple-stub matching network with $250\mu\text{m}$ unit-cells. These circuits show the substantial benefit of one-dimensional realizations of this concept; a discussion of a two-dimensional implementation circuit, a switch matrix, follows and is accompanied by a comparison with state-of-the-art switches. Demonstration of a two-dimensional reconfigurable circuit is left as future work.

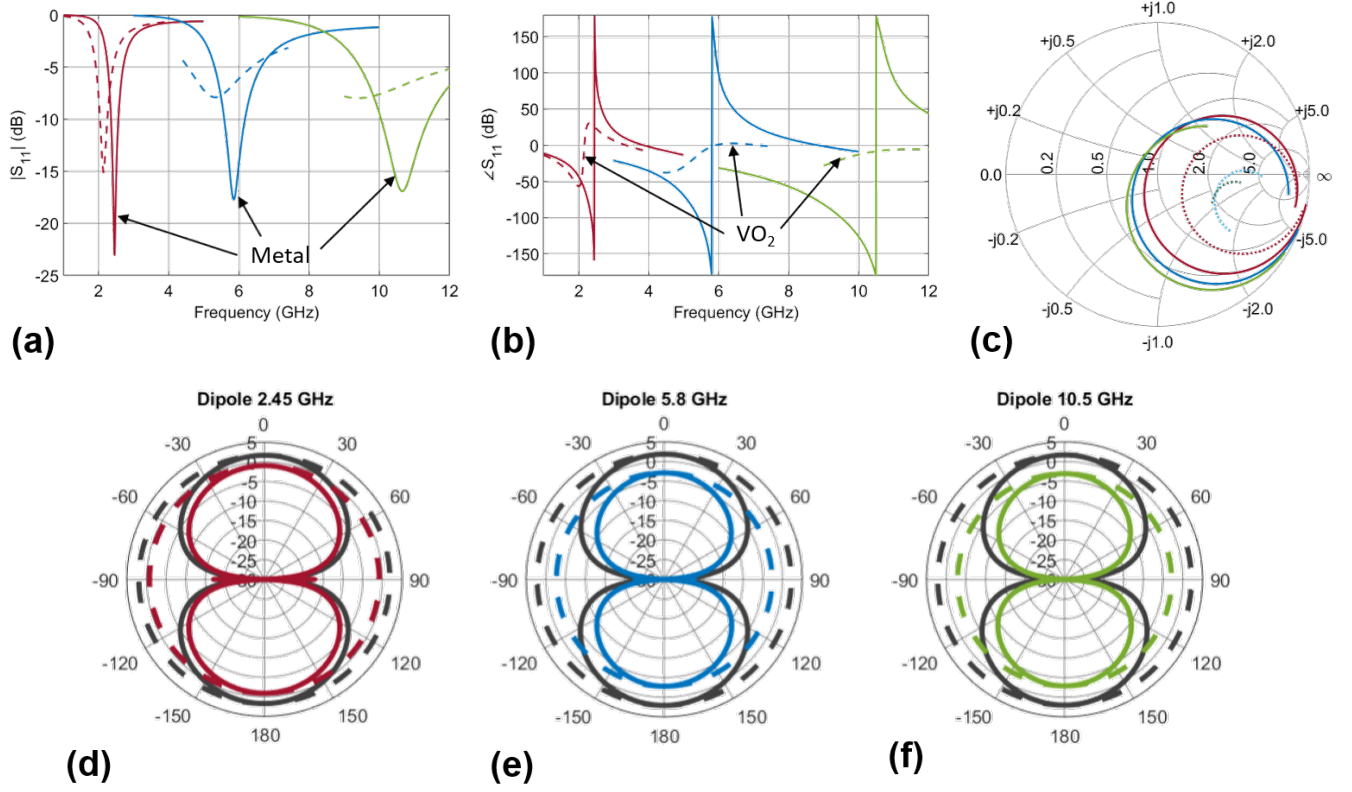


Fig. 12. (a), (b), and (c) plot the magnitude, phase and impedance of each metal (solid) and VO₂ dipole (dashed): red is 2.45 GHz, blue is 5.8 GHz, green is 10.5 GHz. d) Radiation patterns are gain patterns for phi cuts 0 (solid) and 90 (dashed). Black is metal and colored is dipole.

A. Reconfigurable Dipole Antenna

Fig. 11 shows a simulation model of a reconfigurable VO₂-metal surface-inclusion dipole from 2.45 to 10.5 GHz. In this section we simulate it and compare its performance with an all-metal versions. The metal dipoles were sized at 38, 14.16, and 7.06 mm in order to be resonant at 2.45, 5.8, and 10.5 GHz. The VO₂ dipoles, comprising ON-state unit-cells, are of the same physical length, but also include OFF-state unit-cells at the ends to emulate a realistic reconfigurable dipole. This adds to their physical and electrical length so that they resonate at 2.13, 5.24, and 9.07 GHz. A VO₂ film thickness of 100 nm, gap of 100 nm, and dipole width of 200 μ m were selected. The dipole was modeled with $\sigma_{\text{ON}} = 10^5$ S/m for ON-state unit-cells and $\sigma_{\text{OFF}} = 80$ S/m for OFF-state unit-cells. The simulation results are shown in Fig. 12. In order to focus on the performance of the VO₂ dipole, it was excited directly at the feed and not with a transmission line; the feeding element is left as an independent task.

In general the VO₂ dipoles exhibit reasonable match and a dipole radiation pattern at each frequency but they resonate with a lower Q, at a slightly lower frequency, with less gain, and higher input impedance than their metal counterparts. Figure 12(a) and (b) show the shift in frequency and damping of the resonance. The shift is attributed to the increased capacitance at the ends of the dipole due to the OFF-state unit-cells, giving the VO₂ dipole a longer electrical length. The damped resonance is attributed to the increase in conductor

TABLE IV
SIMULATED METAL AND VO₂ DIPOLE ANTENNA AND CIRCUIT PARAMETERS

Dipole (GHz)	D ₀ (dBi)	G ₀ (dBi)	η_{cd}	R _r (Ω)	R _s (Ω)	L (nH)	C (fF)	C _f (fF)
Metal 2.45	2.09	1.71	0.917	39.6	3.6	23.3	183	137
Metal 5.8	2.19	2.07	0.973	34.9	0.96	6.78	114	137
Metal 10.5	2.09	2.00	0.979	28.8	0.62	2.94	81.7	137
VO ₂ 2.13	-0.25	-0.93	0.855	60.5	10.3	26.5	210	151
VO ₂ 5.24	2.25	-2.81	0.312	36.7	80.7	6.69	138	89.7
VO ₂ 9.07	2.01	-2.90	0.322	35.7	75	2.73	113	68.3

loss from the presence of VO₂. In addition to being damped, the resonance of the 5.8 and 10.5 GHz VO₂ dipoles are also shifted capacitively, as seen by the shift towards a negative angle in the resonance's center point, and the rotation on the Smith chart (Fig. 12(c)) about a more capacitive impedance point. This higher and more capacitive input impedance is indicative of a change in the current at the input terminals, which is influenced by both the OFF-state unit-cells terminating the dipole as well as the gap capacitance and VO₂ resistance of each ON-state unit-cell.

The circuit model fit (Fig. 11(c)) bears the above trends out as well and is documented in Table IV. Specifically, both the conductor resistance R_s and the series C significantly increase as compared to the metal dipoles. The $1/\sqrt{LC}$ frequency

where the VO₂ dipole resonances actually occur are 2.13, 5.24, and 9.07 GHz. The smaller the VO₂ dipole, the greater the shift for two reasons: the OFF-state unit-cells have less isolation with higher frequency, and their physical extent comprises a larger fraction of the total length for shorter dipoles.

The VO₂ dipole gain patterns, efficiencies, radiation resistance R_r and the conductor resistance R_s are calculated at 2.13, 5.24, and 9.07 GHz. The gain patterns are identical to the metal patterns in shape, as seen in Fig. 12(d), (e), and (f). The maximum gain is -0.93, -2.81, and -2.9 dBi for each VO₂ dipole, respectively. Since the substrate is sapphire, all losses are attributed to conductor losses. While the gain of these dipoles is lower than an isotropic radiator, this reconfigurable dipole has a 4.25 tuning ratio or 124% bandwidth, rendering it incredibly useful for a wide range of frequencies. Table V compares this approach with several other reconfigurable antenna technologies.

B. Reconfigurable Triple-Stub Matching Network

In addition to the reconfigurable dipole, we have simulated the performance of a triple stub matching network utilizing the circuit models developed from EM simulations of $T_{VO2} = 100$ nm and gap size of $G = 100$ nm from 10 MHz to 50 GHz. Because a triple stub tuner is capable of transforming a source impedance to any region of the Smith chart, this is an excellent one-dimensional application of our PCM-metal surface-inclusion concept. We chose to use the circuit model because (i) this allows us to simulate all possible stub length combinations over a wide band incredibly more efficiently than with EM simulations, (ii) the unit-cell length can easily be varied, and (iii) this demonstrates the usefulness of the circuit models for rapidly prototyping new distributed circuits.

A possible scenario for a triple-stub tuner can be seen in Fig. 13(a), in which a tuner is used to match a power amplifier to an antenna in a dynamic near-field environment. The antenna environment causes significant and possibly rapidly varying changes in the antenna input impedance, which necessitates real-time adjustment to the antenna matching network. This is useful in e.g., mobile phones where antennas must operate in

TABLE V
COMPARISON OF RECONFIGURABLE ANTENNAS

Tech	Freq. (GHz)	Tune (%)	Eff./Gain (%)/(dBi)	Speed (μ sec)	DC Bias
Liquid [29]	4.48-5.52	20.8	90.4/0.3	Slow	N/A
Origami [30]	1.78-3.64	68.6	12.7 dBi	Deployable	N/A
Ferrite [31]	9.75-10.7	9.29	86/6.5	—	200 kA/m
Piezoelec. [32]	2.78-2.98	9	8.3 dBi	—	200 V
Optoelec. [33]	2.65-10.3	118	—	—	590 mW
Sim VO ₂ [9]	2-10	133	-27.5 to -12 dBi	80 msec	121.5 μ W
GeTe [34]	24.4-29	17.2	> 73 / > 3.02	0.03	—
This Work	2.13-9.07	124	0.312 / -2.81	—	—

isolation as well as when brought near a human body or placed on various surfaces. Figure 13(b) shows the simulation setup, where a microstrip triple-stub tuner on a 100 μ m sapphire substrate has stubs that are capable of being reconfigured by selecting the ON or OFF state circuit model. A metal thickness of 2 μ m was used. The tuner was modeled with $\sigma_{ON} = 10^5$ S/m for ON-state unit-cells and $\sigma_{OFF} = 5$ S/m for OFF-state unit-cells. The unit-cell size selected was 250 μ m, and the total number of unit-cells available for tuning on each stub is 30, for a possible 30^3 stub length combinations with only $30 \times 3 = 90$ control heaters (consuming an estimated 36 μ W of power in the heater array). The spacing between each stub is $1/8$ at 5.8 GHz.

Figure 13(c) and (d) show the region covered on the Smith chart for a purely metallic tuner and a reconfigurable VO₂-metal surface-inclusion stub at 5 GHz. While the VO₂ tuning network comes close to the performance of the metallic counterpart, the ON-state loss and OFF-state isolation in the VO₂ reduces slightly the $|\Gamma|$ of the network. Figure 13(e) compares the maximum $|\Gamma|$ of each tuning network: $|\Gamma|_{VO2} = 0.934$, $|\Gamma|_M = 0.981$ at low impedances and $|\Gamma|_{VO2} = 0.861$, $|\Gamma|_M = 0.963$ at high impedances.

Figure 14 shows the performance of the VO₂ matching network at 5, 10, 20, and 40 GHz. The network is still able to capture the majority of the Smith chart with very good

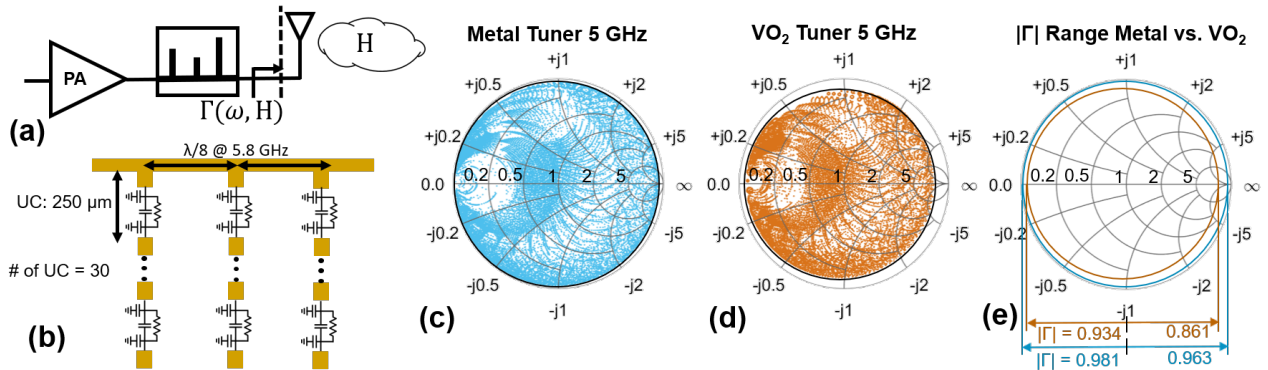


Fig. 13. (a) A VO₂ reconfigurable triple-stub matching network has the potential respond real-time to an antenna's input impedance, which changes not only with frequency but also with the near-field environment, H. (b) The tunable triple stub matching network was simulated with the circuit models extracted from EM simulations of thick VO₂ and microstrip transmission lines. All possible combinations of thirty unit-cells per stub, with a unit-cell length of 250 μ m were simulated and presented in (d). (c) shows the equivalent for a tunable metallic-only triple-stub matching network. (e) compares the maximum $|\Gamma|$ for a purely metallic stub.

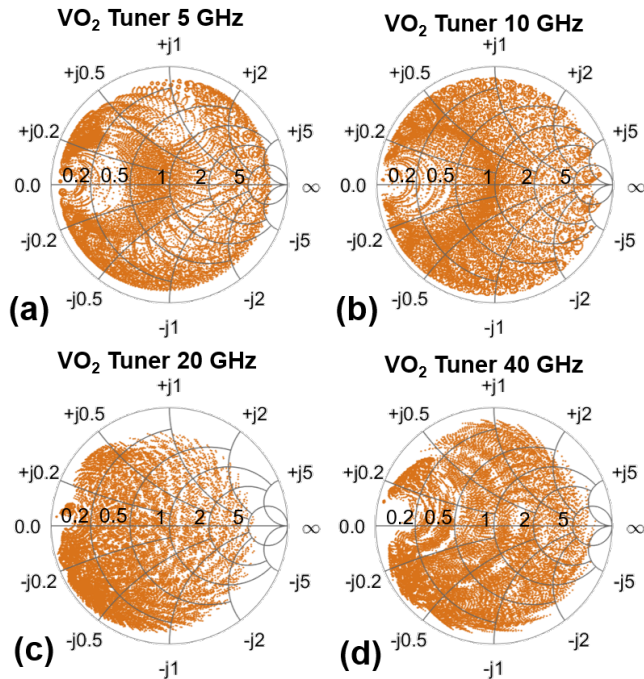


Fig. 14. The VO₂ tunable triple-stub matching network simulated at 5, 10, 20 and 40 GHz.

granularity considering a large unit-cell size of $250\ \mu\text{m}$. At 40 GHz, where $250\ \mu\text{m}$ is 31° of a guided wavelength, the stubs become periodic in $\lambda/2$ after 11 unit-cells. The matching network, however, can still present a different impedance each time the stub's physical length becomes periodic in $\lambda/2$ because of the increase in total loss of the stub. Therefore, this triple-stub matching network has an 8:1 tunable bandwidth.

C. Reconfigurable Switch Matrix

The above one-dimensional demonstrations of reconfigurable circuits testify to the efficacy of this approach by achieving significant reconfigurability within a single application. To obtain full programmability of distributed circuits, a two-dimensional reconfigurable surface is needed. The performance of this reconfigurable surface is fundamentally linked to the primitive's (unit-cell) Figure of Merit (FOM), which means that, even for the best of switches, a reconfigurable surface will never achieve the same performance as a dedicated metallic circuit. Rather, the benefit of a reconfigurable surface with high FOM primitives is that a circuit can be tuned or reconfigured in near-real-time to meet changes in requirements or changes in a radio's environment.

While VO₂ has a high FOM comparable to state-of-the-art switches (see Table VI) and can be controlled by thermal heaters that are electrically isolated from the EM circuit, this concept is not tied to a single switch technology. MEMS switches have the highest FOM but suffer from long-term reliability and high activation voltages. Additionally, designing bias lines for large switch matrices that maintain low EM coupling becomes an extremely challenging task. Germanium telluride (GeTe) has a comparable FOM to VO₂, but has

TABLE VI
COMPARISON WITH SWITCH TECHNOLOGIES

Technology	FOM (THz)	Loss/Isol. (dB)	Freq. (GHz)	Power	Speed (μsec)
VO ₂ [17]	26.5	$<0.5/>30$	DC-50	37.5 mW	0.025
GeTe [35]	7.8	$<0.3/>20$	0-26	No static	0.15-2
FET [36]	0.263	—	0.5-10	60 μW	34.2
MEMS [37]	16.5	$<0.26/>21$	DC-12	63 VDC	7-14
MEMS [38]	63.7	$R_{\text{ON}}/C_{\text{OFF}}=0.22\Omega, 11\text{fF}$	0.2-4	—	—
This work	1.5	$<0.867/>10.5$	DC-10	—	—
This work	36.79	$<0.015/>6.7$	DC-10	$<36\ \mu\text{W}$	—
VO ₂ 35 nm	10.4	$R_{\text{ON}}, C_{\text{OFF}}=3\Omega, 5\text{fF}$	0.01-50	—	—

the advantage of zero static power dissipation with electrical triggering [35]. Furthermore, a PCM film-based approach has the advantage of preserving the mode continuity between unit-cells much more so than a FET, MEMS, or diode would preserve it.

VI. CONCLUSION

We have characterized, for the first time, transmission lines made of thin VO₂ films with metallic inclusions and have found that thicker films (100–200 nm) and lower percentage of VO₂ ($\ll 5\%$) are required to realize low-loss reconfigurable distributed circuits. While this blend of PCM material and metal is the first step in enabling low-loss, fully programmable distributed circuits, the trade-off is a reduction in current confinement that degrades with frequency. We have also successfully modeled these structures with EM simulations, and have extracted both a transmission line model at 50 GHz and a lumped-element circuit model of the VO₂ gaps that is valid from 0.01–50 GHz. We have concluded with a demonstration of a reconfigurable dipole at 2.14, 5.24, and 9.07 GHz, and a tunable matching network with high- $|\Gamma|$ at 5, 10, 20, and 40 GHz. Arbitrary 2D designs will benefit from our EM model parameters for full-wave simulations, whereas 1D structures can be rapidly prototyped using the transmission line and circuit model parameters.

Future work to expand this concept to 2D will require studying the characteristic impedance of poorly defined conductors as well as investigating and comparing the performance of different waveguides. Microstrip, for example, is likely to perform better than planar waveguides, such as slotlines and CPW, given that the entire ground plane can remain metal and that the OFF-state VO₂ will not increase shunt conductance between signal and ground.

VII. ACKNOWLEDGEMENTS

The authors gratefully acknowledge help from Professor R. Engel-Herbert at Pennsylvania State University for supplying the VO₂ samples. The authors would also like to thank Edit Varga for assistance with AFM measurements, and Nicholas Estes for helpful conversations about VO₂.

REFERENCES

- [1] V. Thry, A. Boulle, A. Crunteanu, J. C. Orlianges, A. Beaumont, R. Mayet, A. Mennai, F. Cosset, A. Bessaoudou, and M. Fabert, "Structural and electrical properties of large area epitaxial vo2 films grown by electron beam evaporation," *J. Appl. Phys.*, vol. 121, no. 5, p. 055303, Feb 2017. [Online]. Available: <https://doi.org/10.1063/1.4975117>
- [2] N. Shukla, A. V. Thathachary, A. Agrawal, H. Paik, A. Aziz, D. G. Schlom, S. K. Gupta, R. Engel-Herbert, and S. Datta, "A steep-slope transistor based on abrupt electronic phase transition," *Nature Comm.*, vol. 6, p. 8812, Aug 2015.
- [3] D. Tomer and R. A. Coutu, "A phase change material for reconfigurable circuit applications," *Appl. Sci.*, vol. 8, no. 1, 2018. [Online]. Available: <http://www.mdpi.com/2076-3417/8/1/130>
- [4] C. Hillman, P. A. Stupar, and Z. Griffith, "Vo2 switches for millimeter and submillimeter-wave applications," in *2015 IEEE Compound Semiconductor Integrated Circuit Symp. (CSICS)*, 2016.
- [5] C. G. R. H. Olsson, K. Bunch and N. Zhou, "Creating a universal radio frequency front-end for elemental digital beam formed phased arrays," in *2016 IEEE Int. Symp. on Phased Array Syst. and Techn. (PAST)*, 2016, pp. 1–4.
- [6] W. A. Vitale, L. Petit, C. F. Moldovan, M. Fernandez-Bolaos, A. Paone, A. Schler, and A. M. Ionescu, "Electrothermal actuation of vanadium dioxide for tunable capacitors and microwave filters with integrated microheaters," *Sensors and Actuators A: Physical*, vol. 241, pp. 245–253, Apr 2016. [Online]. Available: <http://www.sciencedirect.com/science/article/pii/S0924424716300279>
- [7] H.-T. Zhang, L. Guo, G. Stone, L. Zhang, Y.-X. Zheng, E. Freeman, D. W. Keefer, S. Chaudhuri, H. Paik, J. A. Moyer, M. Barth, D. G. Schlom, J. V. Badding, S. Datta, V. Gopalan, and R. Engel-Herbert, "Imprinting of local metallic states into vo2 with ultraviolet light," *Adv. Funct. Mat.*, vol. 26, no. 36, pp. 6612–6618, 2016. [Online]. Available: <https://onlinelibrary.wiley.com/doi/abs/10.1002/adfm.201601890>
- [8] H. Frey and H. Khan, *Handbook of thin film technology*. Heidelberg: Springer-Verlag Berlin Heidelberg, 2015, p. 144.
- [9] B. Gerislioglu, A. Ahmadivand, M. Karabiyyik, R. Sinha, and N. Pala, "Vo2-based reconfigurable antenna platform with addressable microheater matrix," *Advanced Electronic Materials*, vol. 3, no. 9, p. 1700170, 2017. [Online]. Available: <https://onlinelibrary.wiley.com/doi/abs/10.1002/aeml.201700170>
- [10] N. Pala, B. Gerislioglu, A. Ahmadivand, and M. Karabiyyik, "Phase-change material based reconfigurable antenna," Mar. 2018, uS Patent 9,923,267 B1. [Online]. Available: <http://www.google.com/patents/US9923267>
- [11] M. Ali, N. Bishop, W. Baron, B. Smyers, J. Tuss, and D. Zeppetella, "A mems reconfigurable pixel microstrip patch antenna for conformal load bearing antenna structures (clas) concept," in *2014 IEEE Antennas and Propagation Society International Symposium (APSURSI)*, July 2014, pp. 1093–1094.
- [12] T. N. Jackson, "Actively reconfigurable pixelized antenna systems," Apr. 2006, uS Patent 6,885,345 B2. [Online]. Available: <http://www.google.com/patents/US6885345>
- [13] L. Chau, J. G. Ho, X. Lan, G. Altvater, R. M. Young, N. El-Hinnawy, D. Nichols, J. Volakis, and N. Ghalichechian, "Optically controlled GeTe phase change switch and its applications in reconfigurable antenna arrays," in *Open Architecture/Open Business Model Net-Centric Systems and Defense Transformation 2015*, R. Suresh, Ed., vol. 9479, International Society for Optics and Photonics. SPIE, 2015, pp. 8 – 15. [Online]. Available: <https://doi.org/10.1117/12.2179852>
- [14] J. Schaffner, H. Song, K. Sayyah, P. Patterson, J.-S. Moon, A. Reamon, K. Kona, and J. Colburn, "Reconfigurable electromagnetic surface of pixelated metal patches," Jan. 2016, uS Patent 2016/0013549 A1. [Online]. Available: <http://www.google.com/patents/US20160013549>
- [15] H.-T. Zhang, L. Zhang, D. Mukherjee, Y.-X. Zheng, R. C. Haislmaier, N. Alem, and R. Engel-Herbert, "Wafer-scale growth of vo2 thin films using a combinatorial approach," *Nature Comm.*, vol. 6, p. 9476, Oct 2015.
- [16] L. Chen, Z. Xiang, C. Tinsman, T. Asaba, Q. Huang, H. Zhou, and L. Li, "Enhancement of thermal conductivity across the metal-insulator transition in vanadium dioxide," *Applied Physics Letters*, vol. 113, no. 6, p. 061902, Aug 2018. [Online]. Available: <https://aip.scitation.org/doi/10.1063/1.5042089>
- [17] H. Madan, H. T. Zhang, M. Jerry, D. Mukherjee, N. Alem, R. Engel-Herbert, and S. Datta, "26.5 Terahertz electrically triggered RF switch on epitaxial VO2-on-Sapphire (VOS) wafer," in *2015 IEEE International Electron Devices Meeting (IEDM)*, Dec. 2015.
- [18] J. R. Mruk, W. N. Kefauver, and D. S. Filipovic, "Band rejection methods for planar log-periodic antennas," *IEEE Trans. on Ant. and Propag.*, vol. 58, no. 7, pp. 2288–2294, Jul. 2010.
- [19] R. Percy, "Characterization and development of submillimeter wavelength devices incorporating vanadium dioxide thin films," Ph.D. dissertation, University of Virginia, 2013.
- [20] M. Naghed and I. Wolff, "Equivalent capacitances of coplanar waveguide discontinuities and interdigitated capacitors using a three-dimensional finite difference method," *IEEE Transactions on Microwave Theory and Techniques*, vol. 38, no. 12, pp. 1808–1815, Dec 1990.
- [21] S. Gevorgian, A. Deleniv, T. Martinsson, S. Gal'chenko, P. Linnr, and I. Vendik, "CAD model of a gap in a coplanar waveguide," *International Journal of Microwave and Millimeter-Wave Computer-Aided Engineering*, vol. 6, no. 5, pp. 369–377, 1996.
- [22] P. Heymann, H. Prinzler, and F. Schnieder, "De-embedding of mmic transmission-line measurements," in *1994 IEEE MTT-S International Microwave Symposium Digest (Cat. No.94CH3389-4)*, May 1994, pp. 1045–1048 vol.2.
- [23] A. Mangan, S. Voinigescu, Ming-Ta Yang, and M. Tazlauanu, "De-embedding transmission line measurements for accurate modeling of IC designs," *IEEE Transactions on Electron Devices*, vol. 53, no. 2, pp. 235–241, Feb 2006. [Online]. Available: <http://ieeexplore.ieee.org/document/1580859/>
- [24] W. H. Haydl, W. Heinrich, R. Bosch, M. Schlechtweg, P. Tasker, and J. Braunstein, "Design data for millimeter wave coplanar circuits," in *1993 23rd European Microwave Conference*, Sept 1993, pp. 223–228.
- [25] N. Garcia, W. Bai, T. Twahirwa, D. Connelly, and J. Chisum, "Silicon micromachined high-contrast artificial dielectrics for millimeter-wave transformation optics antennas," in *2017 IEEE International Symposium on Antennas and Propagation USNC/URSI National Radio Science Meeting*, July 2017, pp. 1971–1972.
- [26] D. M. Pozar, S. D. Targonski, and H. D. Syrigos, "Design of millimeter wave microstrip reflectarrays," *IEEE Transactions on Antennas and Propagation*, vol. 45, no. 2, pp. 287–296, Feb 1997.
- [27] A. Papathanasopoulos, Y. Rahmat-Samii, N. Garcia, and J. D. Chisum, "A novel collapsible flat-layered metamaterial gradient-refractive-index (grin) lens antenna," *IEEE Transactions on Antennas and Propagation*, pp. 1–1, 2019.
- [28] T. Vaha-Heikkilä, J. Varis, J. Tuovinen, and G. M. Rebeiz, "W-band rf mems double and triple-stub impedance tuners," in *IEEE MTT-S International Microwave Symposium Digest, 2005.*, June 2005, pp. 4 pp–926.
- [29] A. M. Morishita, C. K. Y. Kitamura, A. T. Ohta, and W. A. Shiroma, "A liquid-metal monopole array with tunable frequency, gain, and beam steering," *IEEE Ant. and Wireless Prop. Lett.*, vol. 12, pp. 1388–1391, 2013.
- [30] S. Yao, X. Liu, S. V. Georgakopoulos, and M. M. Tentzeris, "A novel tunable origami accordion antenna," in *2014 IEEE Ant. and Propag. Soc. Intl. Symp. (APSURSI)*, 2014, pp. 370–371.
- [31] L.-R. Tan, R.-X. Wu, C.-Y. Wang, and Y. Poo, "Ferrite-loaded SIW bowtie slot antenna with broadband frequency tunability," *IEEE Antennas and Wireless Propagation Letters*, vol. 13, pp. 325–328, 2014.
- [32] J. Bernhard, E. Kiely, and G. Washington, "A smart mechanically actuated two-layer electromagnetically coupled microstrip antenna with variable frequency, bandwidth, and antenna gain," *IEEE Transactions on Antennas and Propagation*, vol. 49, no. 4, pp. 597–601, Apr 2001.
- [33] G. Jin, D. Zhang, and R. Li, "Optically controlled reconfigurable antenna for cognitive radio applications," *Electronics Letters*, vol. 47, no. 17, pp. 948–950, Aug 2011.
- [34] L. Huitema, J. L. Valdes, H. Wong, and A. Crunteanu, "Optical switching of GeTe phase change material: Application to a frequency agile millimeter-waves patch antenna," in *12th European Conference on Antennas and Propagation (EuCAP 2018)*, Apr 2018, pp. 1–5.
- [35] T. Singh and R. R. Mansour, "Chalcogenide phase change material GeTe based inline RF SPST series and shunt switches," in *2018 IEEE MTT-S International Microwave Workshop Series on Advanced Materials and Processes for RF and THz Applications (IMWS-AMP)*, Jul 2018, pp. 1–3.
- [36] A. Botula, A. Joseph, J. Slinkman, R. Wolf, Z.-X. He, D. Ioannou, L. Wagner, M. Gordon, M. Abou-Khalil, R. Phelps, M. Gautsch, W. Abadeer, D. Harmon, M. Levy, J. Benoit, and J. Dunn, "A thin-film SOI 180nm CMOS RF switch technology," in *2009 IEEE Topical Meeting on Silicon Monolithic Integrated Circuits in RF Systems*, Jan 2009, pp. 1–4, ISSN: null.
- [37] S. Dey, S. K. Koul, A. K. Poddar, and U. L. Rohde, "Extensive performance evaluations of RF MEMS single-pole-multi-throw (SP3t

to SP14t) switches up to x-band frequency,” *Journal of Micromechanics and Microengineering*, vol. 27, no. 1, p. 014002, Nov 2016.

- [38] P. Grant, M. Denhoff, and R. Mansour, “A Comparison between RF MEMS Switches and Semiconductor Switches,” in *2004 International Conference on MEMS, NANO and Smart Systems (ICMENS’04)*, Aug. 2004, pp. 515–521.



David A. Connelly (Student Member, IEEE) is currently a Ph.D student in Electrical Engineering at the University of Notre Dame in Indiana, U.S.A. In 2016, he graduated with a B.S., Electrical Concentration from LeTourneau University in Longview, Texas, U.S.A. His research interests are in exploiting novel materials, including phase change materials, and magnetic spin-waves for RF signal processing and control.



Jonathan D. Chisum (S’02–M’06–SM’17) received the Ph.D. in Electrical Engineering from the University of Colorado at Boulder in Boulder, Colorado USA, in 2011.

From 2012 to 2015 he was a Member of Technical Staff at the Massachusetts Institute of Technology Lincoln Laboratory in the Wideband Communications and Spectrum Operations groups. His work at Lincoln Laboratory focused on millimeter-wave phased arrays, antennas, and transceiver design for electronic warfare applications. In 2015 he joined the

faculty of the University of Notre Dame where he is currently an Assistant Professor of Electrical Engineering. His research interests include millimeter-wave communications and spectrum sensing with an emphasis on low-power and low-cost technologies. His group focuses on gradient index (GRIN) lenses for low-power millimeter-wave beam-steering antennas, nonlinear (1-bit) radio architectures for highly efficient communications and sensing up through millimeter-waves, as well as reconfigurable RF circuits for wideband distributed circuits and antennas.

Dr. Chisum is a senior member of the IEEE, a member of the American Physical Society, and an elected Member of the U.S. National Committee (USNC) of the International Union of Radio Science’s (URSI) Commission D (electronics and photonics). He is the past Secretary and current Vice-chair for USNC URSI Commission D: Electronics and Photonics.